*J Mater Sci: Mater Electron* (2024) 35:1163

# Novel photocatalyst for fast treatment of ciprofloxacin and crystal violet pollutants: $In^{3+}$-doped $CuO/CuMn_2O_4$ nanocomposite

Nabil Al-Zaqri[1,*] and Abeer A. AlObaid[1]

[1] *Department of Chemistry, College of Science, King Saud University, P.O. Box 2455, 11451 Riyadh, Saudi Arabia*

**Received:** 6 February 2024
**Accepted:** 6 June 2024

© The Author(s), under exclusive licence to Springer Science+Business Media, LLC, part of Springer Nature, 2024

## ABSTRACT

Removal of organic pollutants by adsorption/visible light photocatalysis is a promising strategy for wastewater treatment. Pure and In-doped $CuO/CuMn_2O_4$ nanocomposites were prepared via a simple sol–gel method. The X-ray diffraction (XRD) analysis proved the formation of nanocrystalline $CuO/CuMn_2O_4$ nanocomposites without any impurities. The addition of $In^{3+}$ ions to $CuO/CuMn_2O_4$ leads to formation of fine grains. Besides, the doping by $In^{3+}$ ions enhances the harvesting of visible light energy of $CuO/CuMn_2O_4$ nanocomposite. In-doped $CuO/CuMn_2O_4$ sample exhibited a huge dielectric permittivity with estimated value of 43,306 at the lowest frequency. For environmental applications, In-doped $CuO/CuMn_2O_4$ catalyst revealed fast photodegradation efficiencies of 97 and 95% for crystal violet and ciprofloxacin contaminants after 25 min of solar irradiation, respectively. The total organic carbon (TOC) and chemical oxygen demand (COD) analyses confirmed the perfect mineralization of crystal violet and ciprofloxacin compounds to carbon dioxide ($CO_2$) and water ($H_2O$) molecules. The measured results demonstrated that the In-doped $CuO/CuMn_2O_4$ nanocomposite has multifunctional properties for electrical storage devices and treatment of organic wastewater.

## 1 Introduction

Modern agriculture, medical and industrial activities use billions of tons of chemical compounds such as pesticides, insecticides, antibiotics and dyes to rise the crop production, protect human and plants and also to fabricate high quality colored products [1–4]. Antibiotics as medical drugs are used by human to damage and obstruct the growth of bacteria and microbes [5]. In addition, the aquaculture zones and farm animals frequently use the antibiotics as they can protect the fish and animal from bacterial infections and help animal development [3]. Globally, it was reported that nearly 100,000–200,000 tons of antibiotics are consumed every year [6]. Despite of the benefits health and economic effects of the antibiotics, the wrong consume by some people and farmers has caused insubstantial environmental water contamination as well as can develop a resistance in microorganisms [7].

With respect to industrial contaminants, colored dyes are a big family of industrial organic compounds that are used in many fields such as textile, leather,

Address correspondence to E-mail: nalzaqri@ksu.edu.sa

https://doi.org/10.1007/s10854-024-12925-6
Published online: 17 June 2024

paper and paint [8]. Annually, 100,000 types of dyes are produced with a total quantity of more than $7 \times 10^5$ tons [8]. Every year, the textile industries consume 100,000 tons of dyes and approximately 10–15% of these organic dyes are discharged into water streams as a waste [9]. These organic dyes can cause very dangerous concerns for the environment, animals, human and aquatic life due to their high stability as well as they reducing the sunlight penetration and induce carcinogenic diseases [8, 10]. Numerous techniques have been highlighted to treat the wastewater such as oxidation, membrane filtration, biological, flocculation-coagulation, adsorption and photocatalysis [11, 12]. Photocatalysis is an important methodology to treat the organic compounds in wastewater based on simple reactions that happened by utilizing semiconductor catalyst and light energy to damage the molecules of pollutants [13, 14]. Synthesis of catalyst with good adsorption properties can assist the photocatalytic process by bringing the pollutants-molecules to catalyst surface [15–17]. Besides, the catalyst with a high harvesting of visible light energy is practically important for utilizing the free sunlight energy [18, 19]. Furthermore, inhibiting the recombination of the electron hole pairs is an essential factor to reinforce the photocatalytic efficiency [20, 21]. As a result, the fabrication of low cost and stable photocatalysts with high adsorption abilities, perfect visible light absorption and good separation of charge carriers can advance the practical wastewater treatment. Many approaches have been proposed to achieve these advantages including metals and nonmetals doping [22], codoping [23] and composite formation [24].

Both, CuO as a narrow bandgap semiconductor and $CuMn_2O_4$ as a binary manganese-copper spinel oxide were emerged as promising photocatalysts for wastewater remediation [25, 26]. It is expected that the formation of doped nanocomposite from CuO and $CuMn_2O_4$ materials can strongly trigger the photocatalytic properties and reduce the time of the reaction. Indium ($In^{3+}$) as a dopant can spread the visible light absorption and induces the formation of defects which can assist the separation of the charge carriers, leading to remarkable degradation activities. Azam Sobhani [27] investigated the photocatalytic activity of hydrothermal synthesized pure $CuMn_2O_4$/CuO nanocomposite for degradation of malachite green, eriochrome black T, and methyl orange under visible light irradiation. The author found that the pure $CuMn_2O_4$/CuO nanocomposite has a photodegradation efficiency of 73.27% for 10 ppm malachite green dye after 90 min with low activity towards eriochrome black T and methyl orange pollutants.

In this study, we report for first time the effect of Indium ($In^{3+}$) doping on the adsorption and photocatalytic characteristics of CuO/$CuMn_2O_4$ nanocomposite for removal of ciprofloxacin and crystal violet under solar energy irradiation. Ciprofloxacin (CIP) is one of the second-generation antibiotics (fluoroquinolone) and it is a broadspectrum antibiotic which essentially exists in wastewater [28]. Dangerously, the presence and accumulation of antibiotics in water systems help the generation of antibiotic bacterial resistance causing a reduction or disappearing of the efficiency of these drugs. On the other hand, crystal violet (CV) is a triarylmethane dye used in numerous fields such as textile and paper industries, paints, printing inks, fingerprints as well as cell histology [29]. Furthermore, the electrical and dielectric properties of pure and In-doped CuO/$CuMn_2O_4$ nanocomposites were studied for electronic and energy storage applications. The structural, optical and morphological properties of the prepared samples were investigated and discussed. The recorded results indicated that the $In^{3+}$-doped CuO/$CuMn_2O_4$ nanocomposite has fast and superior photo-removal efficiencies (93–97%) for ciprofloxacin antibiotic and crystal violet dye after 25 min of irradiation. As well, the doped composite interestingly has shown a stable giant dielectric permittivity which encourage the use of this composition for microelectronics and energy storage systems.

## 2 Experimental

### 2.1 Synthesis, characterization and electrical measurements

Pure and 5 wt% indium-doped CuO/$CuMn_2O_4$ nanocomposites were synthesized using a sol–gel method. Figure 1 shows a schematic diagram of the synthesis process and chemical compositions. All chemicals including $Cu(NO_3)_2{\cdot}3H_2O$ (99.9%), $Mn(NO_3)_2{\cdot}4H_2O$ (99.9%) and $In(NO_3)_3$ (99.9%) were obtained from Sigma-Aldrich Company. For pure CuO/$CuMn_2O_4$ nanocomposite, 14.5 g of $Cu(NO_3)_2{\cdot}3H_2O$ and 25.1 g of $Mn(NO_3)_2{\cdot}4H_2O$ with molar ratio of 1.2:2 were dissolved into 120 mL deionized water under constant stirring to achieve a mixed solution, respectively. At room temperature, the citric acid ($C_6H_8O_7$) was added

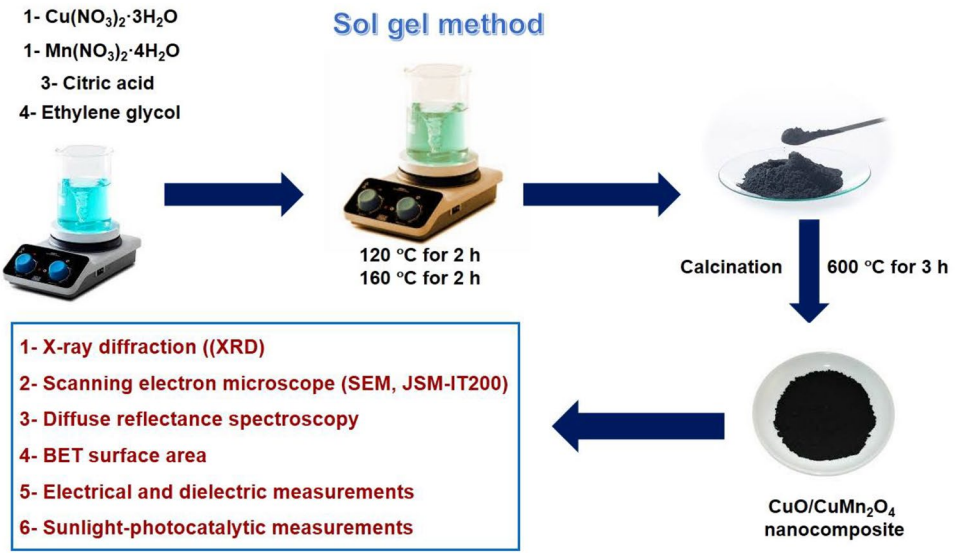



**Fig. 1** shows a schematic diagram of the synthesis process, chemical compositions and measurements

to the solution under constant stirring for 30 min followed by the addition of ethylene glycol. On hotplate, the obtained mixture was stirred at 120 °C for 2 h to form the gel and then the temperature was raised to 160 °C to produce burnet powder. Finally, the powder was calcined in an electric furnace at 600 °C for 3 h. In case of 5 wt% In-doped $CuO/CuMn_2O_4$ nanocomposite, the same steps were used but with dissolving of 0.75 g $In(NO_3)_3$ with 14.137 g of $Cu(NO_3)_2{\cdot}3H_2O$ and 24.47 g of $Mn(NO_3)_2{\cdot}4H_2O$ into 120 mL deionized water. The obtained samples were coded as CC for $CuO/CuMn_2O_4$ nanocomposite and ICC for In-doped $CuO/CuMn_2O_4$ nanocomposite. The obtained powders were characterized by X-ray diffraction (XRD, Bruker D8 Advance diffractometer, $CuK\alpha_1 = 1.5406$ Å) over a 2θ range of 10–80°, scanning electron microscope (SEM, JSM-IT200), diffuse reflectance spectroscopy (DRS, PerkinElmer Lamda-900) and BET surface area using NOVA 3200, USA apparatus. The electrical and dielectric characteristics of pure and In-doped $CuO/CuMn_2O_4$ were measured using LCR apparatus (Hioki 3532–50).

## 2.2 Photocatalytic measurements

The photocatalytic properties of pure and In-doped $CuO/CuMn_2O_4$ nanocomposites were tested for removal of 10 mg/L crystal violet dye and ciprofloxacin antibiotic as common organic pollutants. The influence of the photolysis and adsorption processes were also investigated. The volume of the photocatalytic solution for crystal violet dye or ciprofloxacin was 100 mL and the used catalyst dose was 0.04 g (40 mg) as the best weight. The mixture of the catalyst and pollutant solution was dark stirring for 20 min in closed box. After that the mixture was stirred under sunlight energy in a sunny day (1–3 pm, October, Saudi Arabia) for 25 min. Every five minutes, 3 mL of the illuminated solution was taken with removing of powder by centrifugation at 10,000 rpm for 15 min. Later, the absorbance of the taken solution was measured and the photodegradation efficiency is calculated using Eq. (1) [30]:

$$\text{Photodegradtion (\%)} = \frac{A_0 - A_t}{A_0} \times 100 \quad (1)$$

where $A_0$ is the main absorbance of the crystal violet dye and ciprofloxacin antibiotic while the $A_t$ is the absorbance at certain irradiation times.

# 3 Results and discussion

## 3.1 X-ray diffraction (XRD) study

The purity, composition and crystal structure of the CC and ICC nanocomposites were determined by X-ray diffraction (XRD) technique. Figure 2 displays the XRD patterns of CC and ICC nanocomposites synthesized at 600 °C. The patterns of both composites show the presence of CuO and $CuMn_2O_4$ phases. In Fig. 2a, the XRD peaks which labeled by black circle

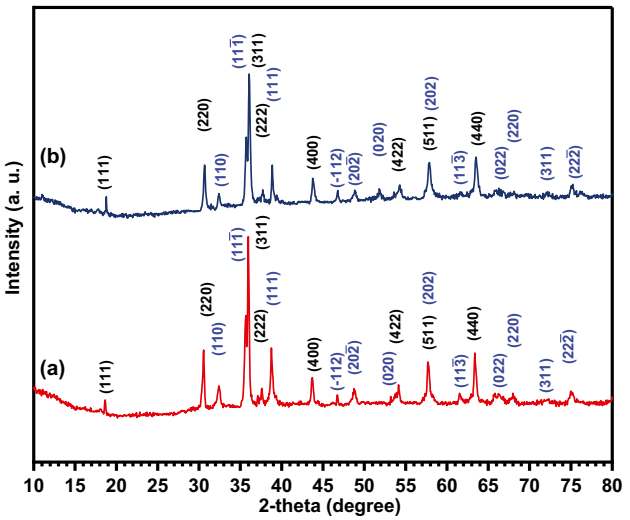



**Fig. 2** X-ay diffraction patterns of **a**: CC composite and **b**: ICC composite

were indexed to monoclinic CuO phase while the XRD peaks labeled by red star were assigned to spinel $CuMn_2O_4$ oxide phase with cubic structure without appearance of any impurities. In more details, the peaks situated at 2-theta = 32.344°, 35.188°, 38.867°, 46.098°, 48.882°, 53.229°, 57.844°, 61.630°, 65.943°, 68.105°, 72.146° and 75.094° were related to (110) (11–1), (111), (-112), (20–2), (020), (202), (11–3), (022), (220), (311) and (22–2) planes of copper oxide (monoclinic phase, JCPDS, card file No. 48–1548, space group: C2/c). On the other hand, the diffraction peaks found at 2-theta = 18.743°, 30.672°, 35.894°, 37.709, 43.789°, 54.278°, 57.844° and 63.520° were attributed to (111), (220), (311), (222), (400), (422), (511) and (440) planes of cubic $CuMn_2O_4$ spinel phase (JCPDS, card file No. 74–1921 space group: Fd-3m). The intense XRD peaks implies that the CC and ICC nanocomposites have a perfect crystallinity. The average crystallite size (D) of the CC and ICC nanocomposites was calculated using the Scherer equation [31, 32], using the most intense XRD peaks of $CuO + CuMn_2O_4$ as demonstrated in Eq. (2):

$$\text{Crystallite size (D)} = 0.9\lambda/\beta\cos\theta \quad (2)$$

The Scherrer equation was used to compute the crystallite size (D) based on XRD analysis through measuring the full width at half maximum of peaks (β) in radian positioned at any 2-theta in the pattern. The shape factor K is usually equal to 0.89, $\lambda$ is the wavelength of the X-ray radiation (CuK$\alpha$ = 0.15406 nm) and θ is the Bragg theta angle of the diffraction peaks in radian. The average crystallite size (D) of CC and ICC nanocomposites was found to be 58 and 53 nm, respectively. Figure 3 shows the crystal structure of ICC nanocomposite based on space filling models of CuO and $CuMn_2O_4$ lattices. The space filling models were plotted to illustrate the coordination of each cation and anion in both phases ($Cu^{2+}$, $Mn^{3+}$ and $O^{2-}$).

## 3.2 Morphological and surface area analysis

Figure 4 illustrates the SEM and corresponding 3D images of CC and ICC nanocomposites synthesized from Cu and Mn nitrates using the sol–gel method. The SEM image of pure $CuO/CuMn_2O_4$ powder displays the formation of some agglomerated

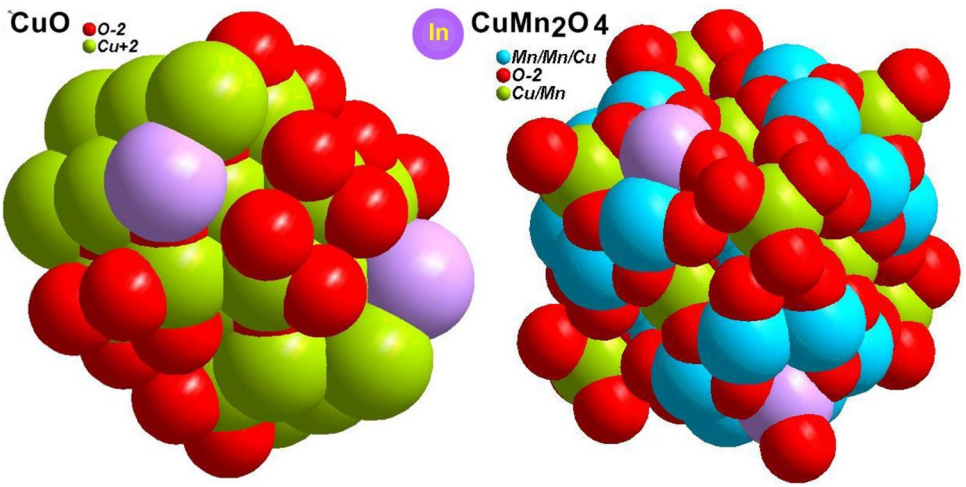



**Fig. 3** Crystal structure of ICC nanocomposite; space filling models of CuO and $CuMn_2O_4$ lattices

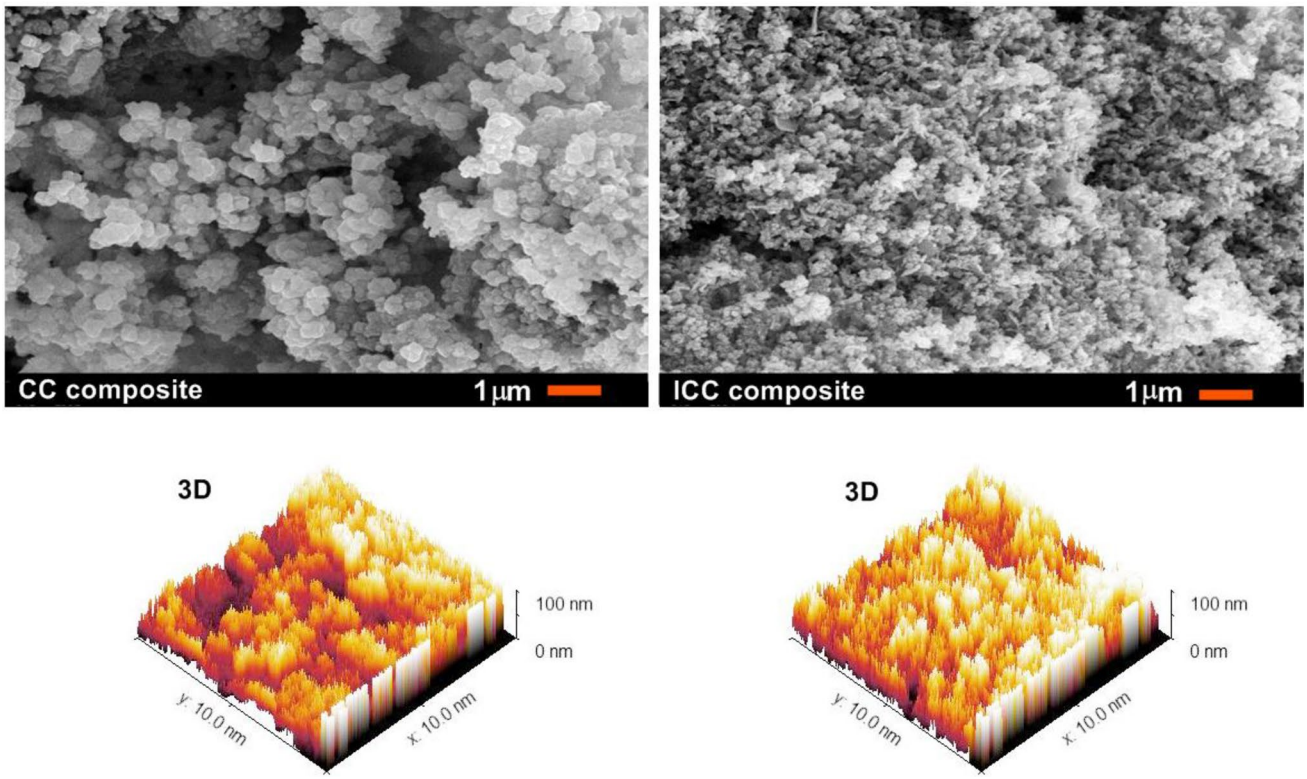



**Fig. 4** Scanning electron microscope (SEM) and 3D images of CC and ICC nanocomposites

semi-spherical particles with moderate homogenous distribution. These semi-spherical grains were mostly fabricated from very fine particles, Fig. 4a. The addition of $In^{3+}$ ions to $CuO/CuMn_2O_4$ composites support the formation of more very finer particles compared to the pure sample. It seems that the occurrence of $In^{3+}$ ions confines the growth of the particles, leading to small particles formation. As depicted in Fig. 4, the 3D images show the regular surface distribution of ICC nanocomposite compared to CC nanocomposite. The EDX spectra of CC and ICC nanocomposites are shown in Fig. 5. Both patterns confirm the presence of essential Cu, Mn, O elements beside indium (In) element in the case of doped composite. The $N_2$ adsorption and desorption isotherms of CC and ICC nanocomposites are shown in Fig. 6, inset pore size distribution curves. The surface area of CC and ICC nanocomposites which is estimated using the BET (Brunauer–Emmett–Teller) was found to be 8.54 and 19.89 $m^2/g$ with total pore volume equal to 0.186 and 0.297 $cm^3/g$. The pore size distribution curves of CC and ICC nanocomposites have an average size of 7 and 12 nm, respectively.

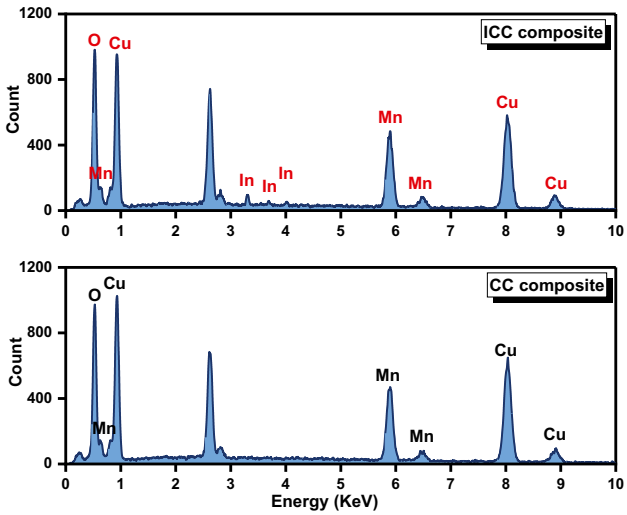



**Fig. 5** Energy dispersive X-ray (EDX) patterns of CC and ICC nanocomposites

These results indicate that the addition of $In^{3+}$ ions to CC composite restricts the grain growth and greatly enhances the surface area which can induce affirmative effects on the interaction between the catalyst

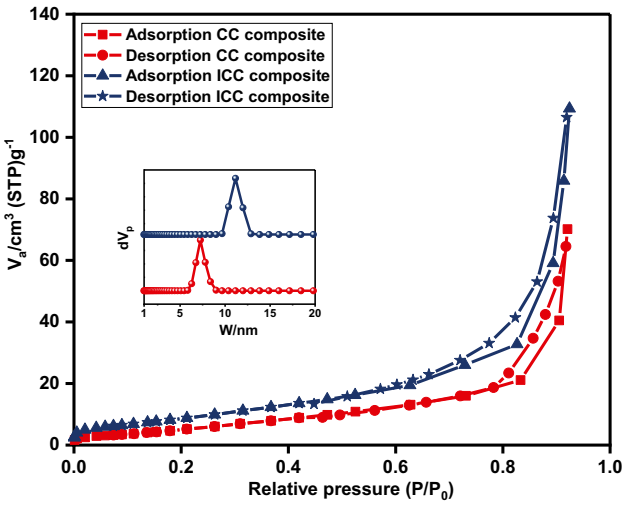



**Fig. 6** $N_2$ adsorption–desorption isotherm of CC and ICC nanocomposites, inset the pore size distribution

particles and the target materials, hence enhancing the photocatalytic efficiency of the CC composite.

### 3.3 Optical properties and response to light energy

The optical features and the bandgap energy of the synthesized catalysts usually determine their efficiencies for elimination of organic waste due to the interaction between catalyst and light energy. Figure 7a demonstrates the change of reflectance (%) with wavelength (300–1500 nm) for CC and ICC nanocomposites. Both samples have two decreases of diffuse reflectance intensity related to the absorption edges of CuO and $CuMn_2O_4$ components as illustrated in Fig. 7a. It can be seen that the absorption edges of ICC composite was shifted to longer wavelength (low energy) compared to pure sample, indicating high harvesting of wavelength for doped sample. To exactly found the energy gap of CC and ICC nanocomposites, the relation of Tauc method was used [33]:

$$\alpha = A(h\upsilon - E_g)^n / h\nu \quad (3)$$

where $\alpha$ is the absorption coefficient, hν signifies the photon energy, A is the independent constant, $E_g$ is the bandgap energy and n is a constant. Using the Kubelka–Munk equation which is represented by the below formula [34]:

$$F(R) = \frac{(1-R)^2}{2R} = \frac{\alpha}{S} \quad (4)$$

In this formula, F (R) is the Kubelka–Munk function, R is the reflectance, and S symbolizes the scattering coefficient. As the scattering coefficient (S) is

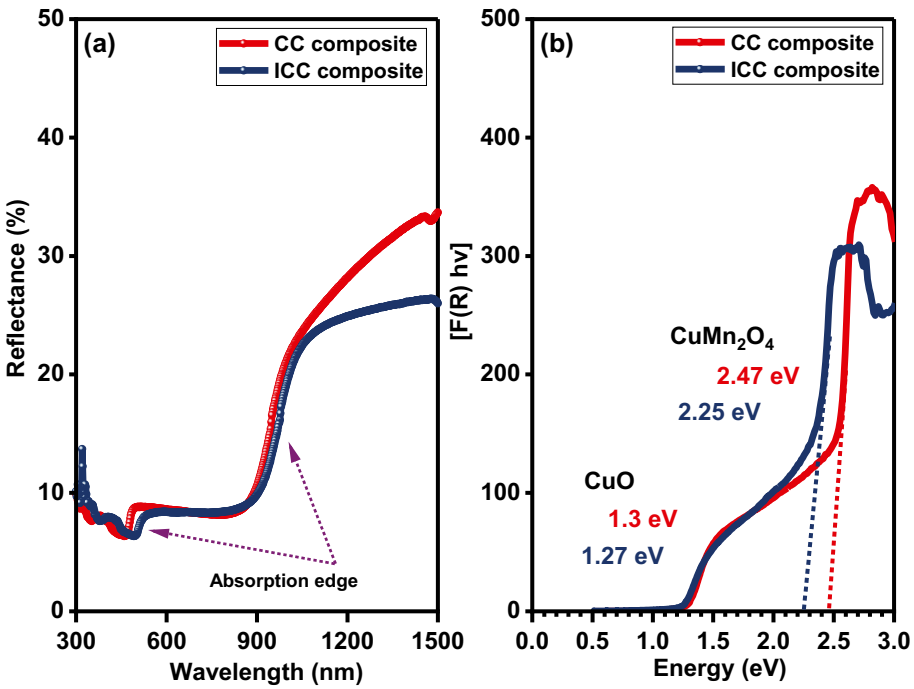



**Fig. 7** Demonstrates **a**: diffuse reflectance spectra and **b**: bandgap of CC and ICC composites

considered as a constant the F(R) can be used instead of $\alpha$ or vice versa. Thus, the plotting of the $[F(R)\ h\nu]^2$ against $h\nu$ (eV) for CC and ICC nanocomposites gives the bandgap energy through lengthening the line part to zero point as shown in Fig. 7 (b). For CC nanocomposite two bandgap energies of 1.3 eV and 2.47 eV were detected which are related to CuO and $CuMn_2O_4$ components, respectively [34, 35]. After insertion of $In^{3+}$ ions into CC nanocomposite, the bandgap energy of CuO was reduced to 1.27 eV while the bandgap energy of $CuMn_2O_4$ component was reduced to 2.25 eV. The reductions of the bandgap energy of both components (CuO and $CuMn_2O_4$) can be assigned to the introducing of impurities states within their bandgap energies [36]. The substitution of $In^{3+}$ for $Cu^{2+}$ sites into CuO or $CuMn_2O_4$ component induce the formation of oxygen vacancies to balance the charge between the two cations ($In^{3+}$, $Cu^{2+}$). In addition, the incorporation of $In^{3+}$ instead of $Cu^{2+}$ sites increases the charge carriers. The formation of oxygen vacancies and the charge carriers may lead to bandgap reduction of both components.

### 3.4 Relative permittivity (dielectric constant) characteristics

Figure 8a shows the results of the dielectric constant with frequency of CC and ICC nanocomposites measured at room temperature. The curve of the pure CC sample displays the rapid decrease of the dielectric constant with increasing the frequency. Giant relative permittivity was found for CC nanocomposite at low frequency region with estimated value of 41,947 at 42 Hz. The dielectric permittivity curve of ICC nanocomposite can be divided into two parts based on frequency values. Within the frequency from 42

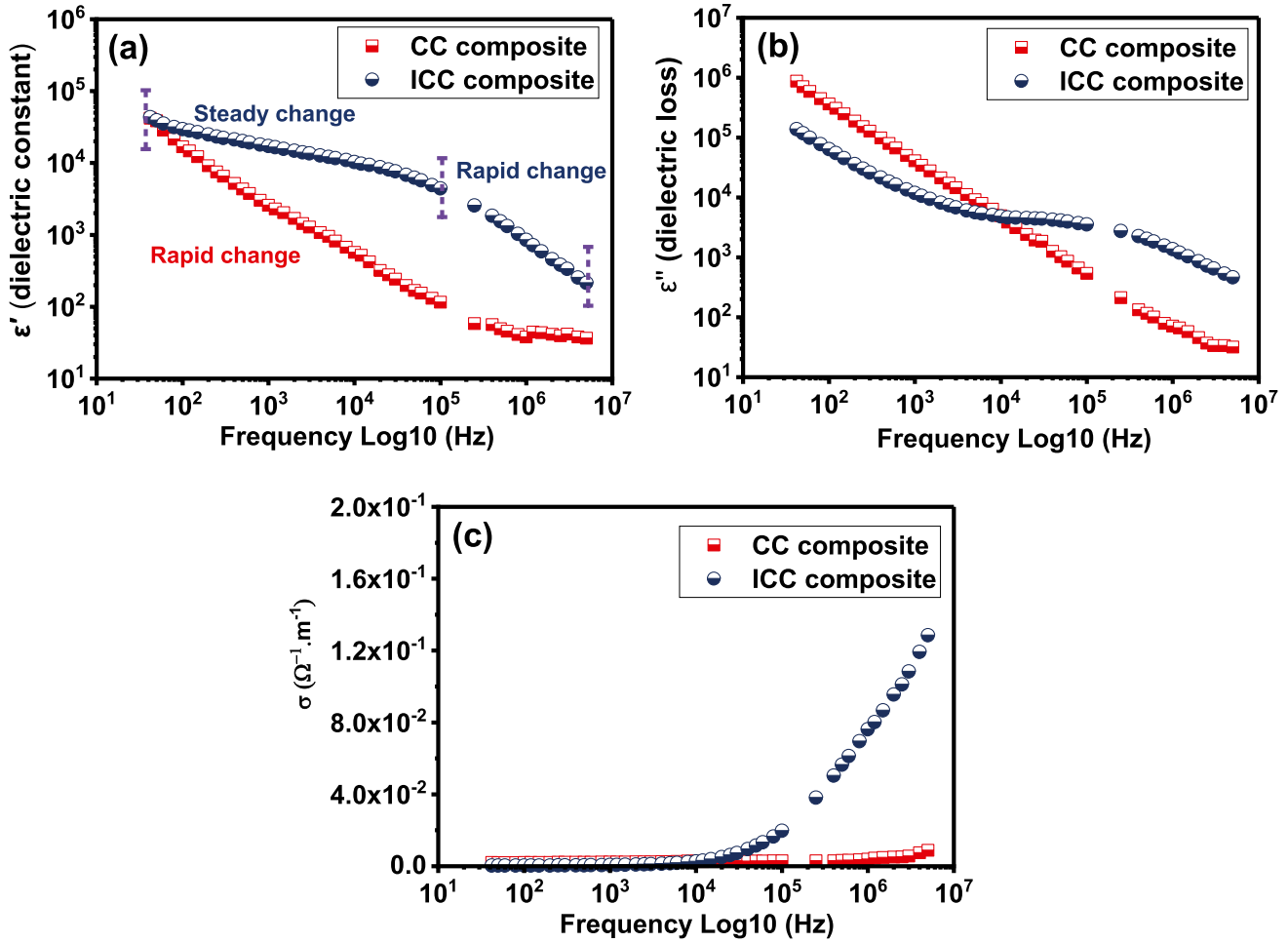



**Fig. 8** Change of **a**: dielectric constant with frequency, **b**: dielectric loss with frequency and **c**: electrical conductivity with frequency of CC and ICC composites

to 100,000 Hz, the dielectric constant value slowly decreased with growing the frequency while above 100,000 Hz the dielectric constant rapidly decreased as illustrated in Fig. 8a. The estimated dielectric constant value of ICC nanocomposite at 42 Hz is equal to 43,306. As seen in Fig. 8a, the embedding of $In^{3+}$ ions significantly enhances the stability of the relative permittivity curve and also maintain the giant values over wide range of frequencies. The stable and giant relative permittivity of ICC nanocomposite are important for applications in capacitance-based energy storage, memory elements and microwave devices. The SEM images show that the addition of $In^{3+}$ ions to $CuO/CuMn_2O_4$ nanocomposite reduces the grains size which consequently increases the grain boundary effect which improve the performance of the permittivity. In addition, the embedding of $In^{3+}$ ions as a replacement for of $Cu^{2+}$ ions leads to formation of Cu vacancies (defects) owing to charge neutrality which assist the improvements of the relative permittivity performance. The Koop's phenomenological and Maxwell–Wagner (MW) theories can be applied to illustrate the frequency-dependent performance of the dielectric constant [37–40]. Based on both models, the composite powders can be presumed as an irregular medium composed of grains which were isolated by weakly conducting grain boundaries, acting as potential barriers. After applying the electric field the electrons travel in the direction of grain boundary through the hopping process. If the resistivity at the grain boundary is very high, the electrons are restricted at the grain boundaries and yield a high polarization, leading to huge dielectric permittivity. However with rise of the applied frequency, the electrons are not capable to follow the interchange of applied field and move in the reverse direction which reduces the polarization. Figure 8b displays the results of the dielectric loss with frequency of CC and ICC nanocomposites. At low frequency, the dielectric loss of ICC composition was lower than that of CC sample which is proper for energy storage uses. The general feature of the curves is the decrease of the dielectric loss with rising the frequency [37–40].

Figure 8c demonstrates the frequency dependence of ac electrical conductivity of CC and ICC nanocomposites. The ac electrical conductivity of both samples increases with increasing the applied frequency which are characteristics for disordered oxides, perovskites and nanocomposites materials. Remarkably, at higher frequencies the ICC nanocomposite has large electrical conductivity values compared to CC composite. The electrical conductivity dependent frequency of CC and ICC nanocomposites can be explained by Koop's model [37–40]. In Koop's phenomenological model, the dispersion of the electrical conductivity occur in higher frequencies (frequency > $10^4$ Hz), which is related to the presence of grains with low resistance and their boundaries with a high resistance. At low frequencies, the change of ac electrical conductivity is described by a static performance independent of the frequency. At low frequencies, this performance is accompanying with the small amplitude of the electrical excitation to produce conductivity through the long-range charge hopping. Above certain specific frequencies, the conductivity start to transfer away from its static performance to a dispersive performance. The dispersive performance can be clarified through considering the applied frequency as a driving force whose growth increases the extraction of the charges which will be trapped in the lattice defects. The replacement of $Cu^{2+}$ sites with $In^{3+}$ ions gives electrons to the conduction band, therefore decreasing the resistivity of the grains, i.e. owing to the donor influence of $In^{3+}$ dopant. Thus, the incorporation of $In^{3+}$ instead of $Cu^{2+}$ sites increases the charge carriers which enhances the electrical conductivity.

### 3.5 Decontamination of crystal violet dye

The effect of adsorption and photocatalytic characteristics of CC and ICC catalysts for removal of 10 mg/L crystal violet dye were investigated under dark and solar illumination, respectively. The influence of photolysis process which represents the self-degradation of crystal violet dye under solar illumination without addition of catalyst was very small (< 0.1%) after 90 min and can be negligible. Figure 9 shows the results of the absorbance and $C_t/C_0$ plots of 10 mg/L crystal violet dye for CC and ICC nanocomposites under dark and solar illumination. Under dark stirring for 20 min, pure CC catalyst showed a low adsorption capacity of 13% while under solar irradiation for 25 min it has a photodegradation efficiency of 59%. In case of ICC catalyst, the adsorption capacity was measured to be 37% (20 min dark stirring) and the photodegradation efficiency was found to be 97% after 25 min of solar illumination. The significant removal characteristics of ICC catalyst compared to pure CC composite can be linked to some factors. Firstly, the SEM and BET studies showed that ICC powder has

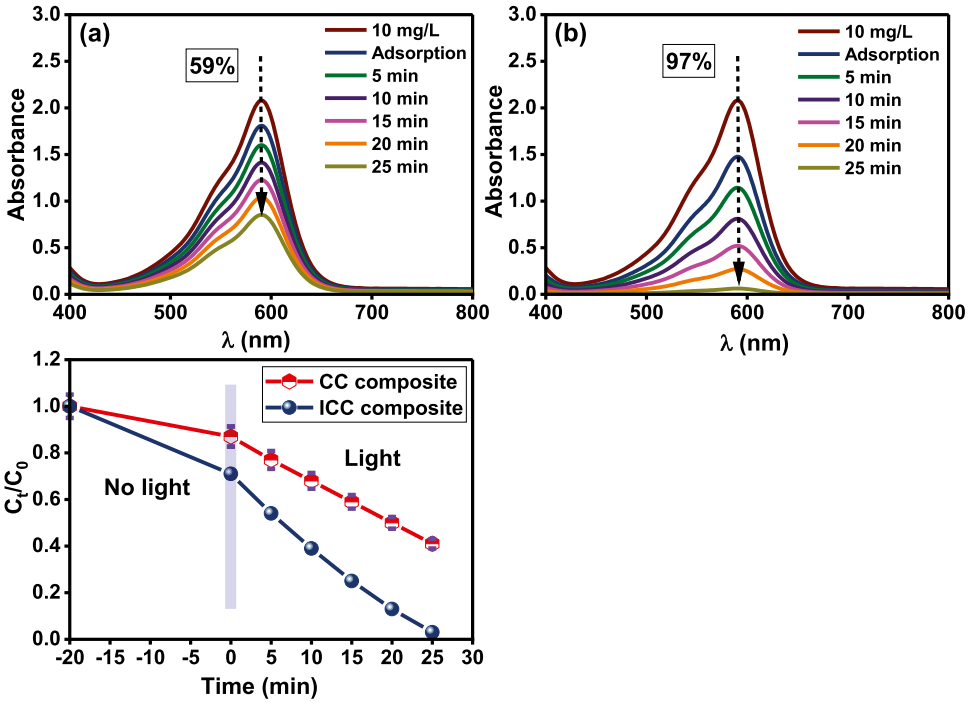



**Fig. 9** Change of absorbance of crystal violet for **a**: CC composite, **b**: ICC composite and **c**: plot of $C_t/C_0$ with time for both samples

more fine particles and large surface area compared to pure composite which consequently increase the surface reaction between catalyst particles and the dye molecules. In addition, the incorporation of $In^{3+}$ ions into $Cu^{2+}$ sites leads to formation of Cu vacancies for charge neutrality. The presence of defects can act as trap centers which hinders the recombination of the electron hole pairs. The optical results indicated that the ICC catalyst possesses a high harvesting for visible light compared to pure CC composite. Besides, the surface interaction between CuO and $CuMn_2O_4$ particles may also support the charge carrier's separation. Furthermore, the integration between the adsorption and photocatalytic leads to this superior performance. These factors can act together to support the efficient removal of crystal violet dye in fast time.

According to non-linear least squares fitting [41], the kinetic performance of CC and ICC nanocomposites is studied as shown in Fig. 10a. The rate constant of CC catalyst was found to be 0.0235 $min^{-1}$ with R-square value of 0.96 while the rate constant of ICC catalyst was estimated to be 0.0354 $min^{-1}$ with R-square of 0.97. In presence of ICC catalyst, the degree of mineralization of crystal violet dye to $H_2O$ and $CO_2$ was analyzed through measuring total organic carbon (TOC%) and chemical oxygen demand (COD%) as illustrated in Fig. 10b. the results of the TOC% and COD% proved that the crystal violet molecules were efficiently mineralized to $H_2O$ and $CO_2$ molecules. The elimination percentages of TOC and COD were increased with increasing the time of the sunlight radiation with recorded mineralization efficiency of 91% and 93% after 40 min, indicating that the ICC catalyst has significant full removal properties. During the photodegradation many active radicals can be produced and to detect these essential species, certain trapping agents (scavengers) were added to the photodegradation reaction. As demonstrated in Fig. 10c, ammonium oxalate (AO), silver nitrate (SN), benzoic acid (BA) and benzoquinone (BQ) were used to trap the hole ($h^+$), electron ($e^-$), hydroxyl (·OH) and superoxide ($^{\cdot}O_2^-$) radicals, respectively [42, 43]. After addition of AO, SN, BA and BQ reagents the photodegradation efficiency of ICC catalyst towards crystal violet dye was reduced to 86, 84, 66 and 58%, respectively. The results reflect that the hydroxyl (·OH) and superoxide ($^{\cdot}O_2^-$) radicals are the basic species which are mainly responsible for the degradation of crystal violet pollutant.

## 3.6 Decontamination of ciprofloxacin antibiotic

Figure 11a and b displays the results of the absorbance and $C_t/C_0$ of 10 mg/L ciprofloxacin antibiotic for ICC catalyst under dark and solar irradiation,

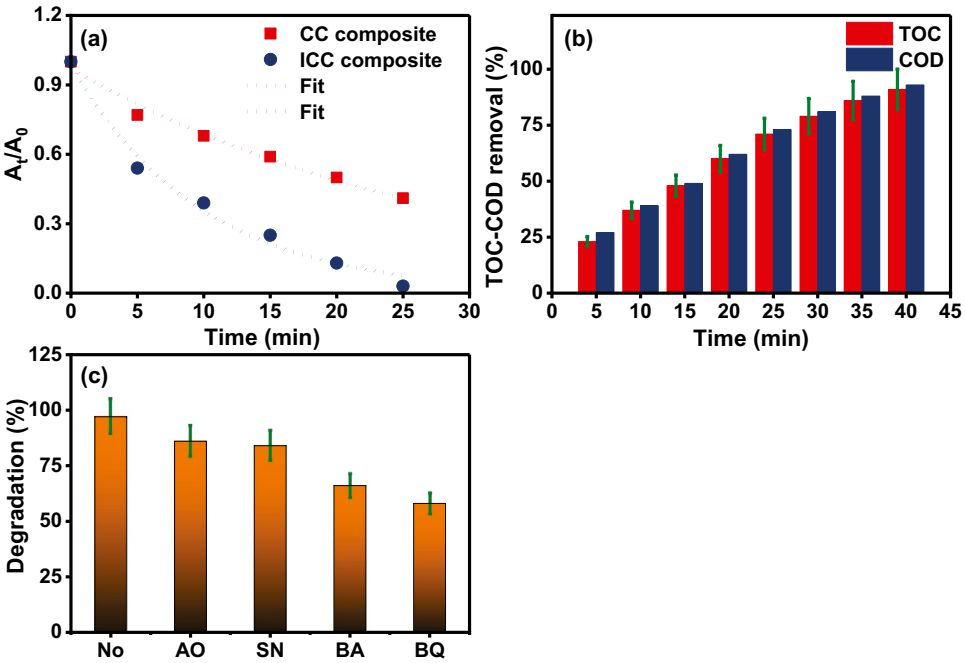



**Fig. 10** Illustrates **a**: kinetic plots of crystal violet dye for both composites, **b**: TOC and COD removal percentage of crystal violet dye for ICC composite and **c**: detection of active radicals for ICC composite

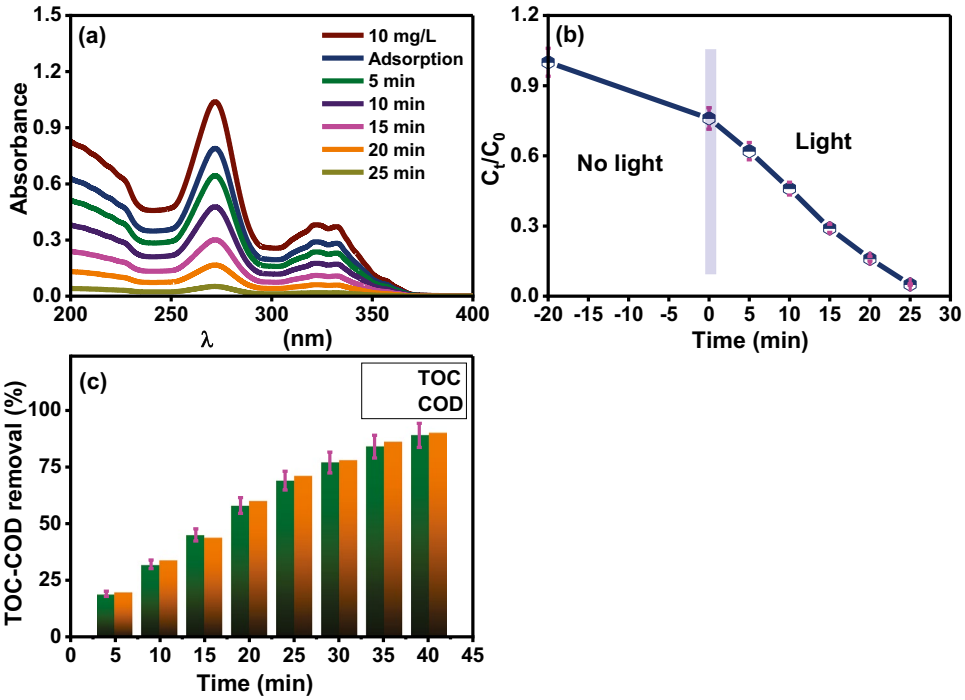



**Fig. 11** **a**: change of absorbance of ciprofloxacin antibiotic, **b**: plot of $C_t/C_0$ with time and **c**: TOC and COD removal percentage of ciprofloxacin for ICC composite

respectively. The absorbance of ciprofloxacin was reduced after dark stirring with measured adsorption capacity of 24% after 20 min. Under solar stirring the absorbance showed further decrease with recorded photodegradation efficiency of 95% after 25 min. As illustrated in Fig. 11c, the TOC% and COD% studies confirmed the effective mineralization of ciprofloxacin molecules to $H_2O$ and $CO_2$ molecules. The measured removal of TOC % and COD % after 40 min reached to 89 and 90%, respectively. The scavengers tests of ICC catalyst toward ciprofloxacin pollutant also indicate that the hydroxyl (·OH)

and superoxide ($^{\cdot}O_2^-$) radicals are the main species during the photodegradation process, Fig. 12a. The reusability experiments of ICC composite for crystal violet and ciprofloxacin contaminants were measured for four runs (successive cycles) as demonstrated in Fig. 12b. After each test the powder of ICC catalyst was collected and then dried to be used for next cycle. The reusability experiments of ICC catalyst for 10 mg/L crystal violet dye was found to be 97, 95, 93 and 90% while the degradation efficiency for ciprofloxacin was estimated to be 95, 94, 90 and 87%, respectively. The photodegradation results for crystal violet dye and ciprofloxacin antibiotic demonstrated that the ICC composite is a promising, efficient and fast catalyst for treatment of organic waste products.

The mechanism of the photo-removal of crystal violet dye and ciprofloxacin antibiotics as organic contaminants models through using ICC catalyst can be discussed based on the above TOC, COD as well as scavengers. The results of the scavenger tests confirmed that the superoxide ($^{\cdot}O_2^-$) and the hydroxyl (·OH) radicals are the main reactive species produced in the photodegradation reaction. The TOC and COD analyses proved the high mineralization of crystal violet dye and ciprofloxacin to $H_2O$ and $CO_2$ molecules. After exposure of ICC catalyst to light energy, the excitation of electron take place, leading to formation of photoexcited electron–hole pairs. Both the electron and hole react with the oxygen and water molecules to produce superoxide ($^{\cdot}O_2^-$) and hydroxyl (·OH) radicals [44–48]. As shown in Fig. 13, both radicals attack the crystal violet and ciprofloxacin molecules and mineralize them as illustrated below:

ICC catalyst + photon energy $\rightarrow e^- + h^+$

$e^- + O_2 \rightarrow {}^{\cdot}O_2^-$.

$h^+ + H_2O \rightarrow \cdot OH + H^+$

$h^+ + OH^- \rightarrow \cdot OH$.

$(\cdot OH/{}^{\cdot}O_2^-)$ + Crystal violet and ciprofloxacin $\rightarrow CO_2 + H_2O$ molecules.

The obtained photodegradation efficiency of ICC catalyst was compared with previous reported results as shown in Table 1. The reported results in Table 1 prove the perfect photodegradation efficiency, low reaction time and the promising photocatalytic characteristics of ICC catalyst for wastewater treatment.

## 4 Conclusion

In this study, indium-doped $CuO/CuMn_2O_4$ nanocomposite was prepared by sol–gel method for energy storage devices and wastewater treatment. The crystal structure analysis proved the production of nanocrystalline $CuO/CuMn_2O_4$ nanocomposites. The incorporation of $In^{3+}$ ions reduced the bandgap of CuO and $CuMn_2O_4$

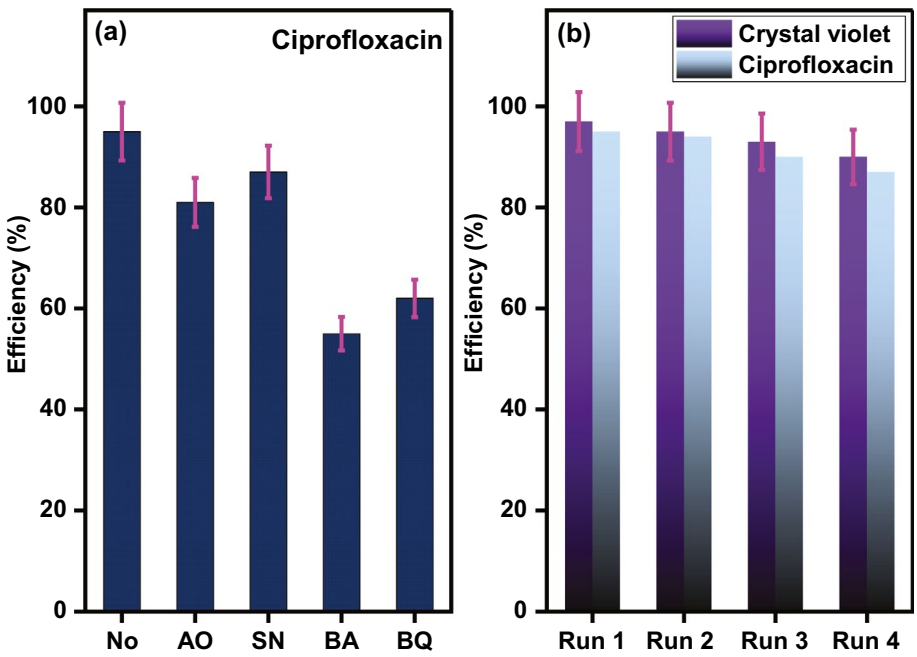



**Fig. 12** **a**: Influence of different trapping agents on the photodegradation efficiency for ciprofloxacin antibiotic and **b**: reusability experiments of ICC composite toward the two crystal violet and ciprofloxacin

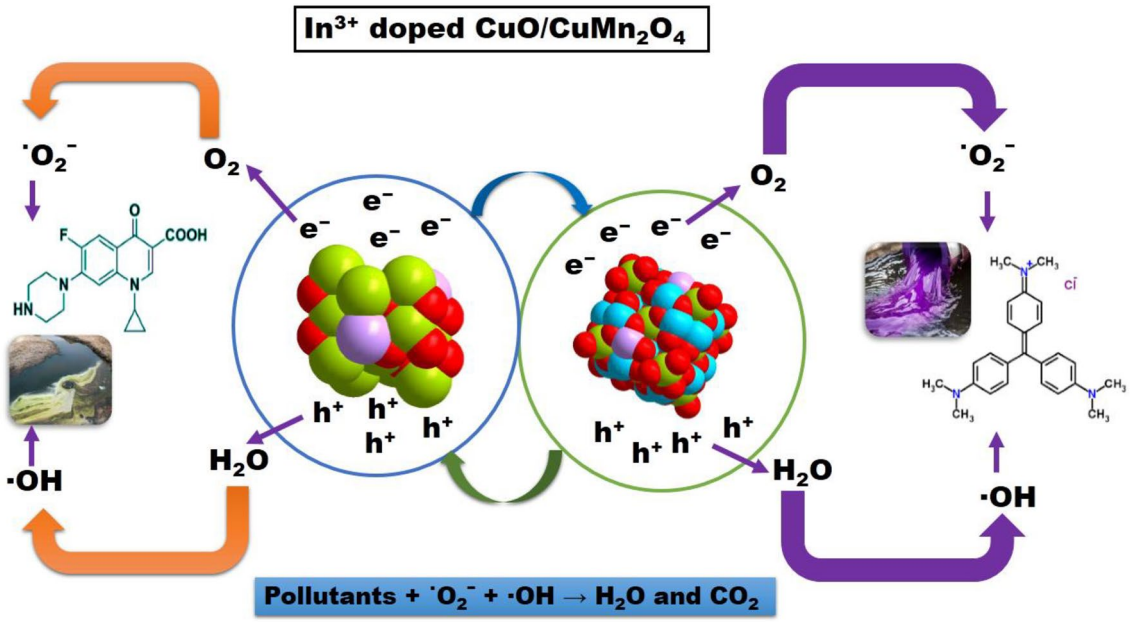



**Fig. 13** Proposed mechanism for photodegradation of crystal violet dye and ciprofloxacin antibiotic in presence of ICC composite

**Table 1** Compare the measured photocatalytic efficiency (%) of ICC composite with previous studies

| Sample | Contaminant | Efficiency (%) | Time (min) | Ref |
|---|---|---|---|---|
| ICC composite | Crystal violet | 97 | 25 | Current |
| | Ciprofloxacin | 95 | 25 | study |
| ZnO/GO nanohybrid | Crystal violet | 99 | 240 | [49] |
| Zr-ZnO | Crystal violet | 100 | 90 | [50] |
| Sr-SnO2 | Crystal violet | 67.8 | 150 | [51] |
| Cr-doped $BaFe_{12}O_{19}$ | Crystal violet | 91 | 90 | [52] |
| Tannin-doped $BaTiO_3$ | ciprofloxacin | 96 | 300 | [53] |
| Zn-doped $Cu_2O$ | ciprofloxacin | 94.6 | 240 | [54] |
| N,S-$TiO_2$ | ciprofloxacin | 78.7 | 150 | [55] |

components which increases the harvesting of visible light spectrum. In-doped $CuO/CuMn_2O_4$ nanocomposite possesses a stable giant dielectric permittivity with measured value of 43,306 at 42 Hz. After 25 min of solar illumination, the removal efficiency of In-doped $CuO/CuMn_2O_4$ catalyst was found to be 97 and 95% for crystal violet and ciprofloxacin pollutants, respectively. Besides, In-doped $CuO/CuMn_2O_4$ catalyst revealed a high stability as well as perfect mineralization properties toward crystal violet and ciprofloxacin pollutants.

## Acknowledgements

The authors extend their appreciation to the Researchers Supporting Project number (RSP2024R381), King Saud University, Riyadh, Saudi Arabia.

## Author contributions

This work was done by Dr. Nabil Al-Zaqri and Abeer A. AlObaid.

## Funding

No funding was received.

## Declarations

**Conflict of interests** The author declares no competing interests.

**Data availability** All relevant data and materials are existing in the main test.

## References

1. S.K. Ponnaiah, P. Periakaruppan, Fabrication of tin oxide and carbon black nanocomposite for effectual electron-hole separation and visible light-harvesting: enhanced photocatalytic degradation of an organophosphorus pesticide. Mater. Chem. Phys. **313**, 128806 (2024). https://doi.org/10.1016/j.matchemphys.2023.128806
2. S.R. Tariq, Z. Niaz, G.A. Chotana, D. Ahmad, N. Rafique, Photocatalytic degradation of imidacloprid using $Ag_2O$/CuO composites. RSC Adv. **13**, 19326–19334 (2023). https://doi.org/10.1039/D3RA02109B
3. A. Azimi-Fouladi, P. Falak, S.A. Hassanzadeh-Tabrizi, The photodegradation of antibiotics on nano cubic spinel ferrites photocatalytic systems: a review. J. Alloy. Compd. **961**, 171075 (2023). https://doi.org/10.1016/j.jallcom.2023.171075
4. K.A. Khan, A. Shah, J. Nisar, Electrochemical detection and removal of brilliant blue dye via photocatalytic degradation and adsorption using phyto-synthesized nanoparticles. RSC Adv. **14**, 2504–3251 (2024). https://doi.org/10.1039/D3RA07519B
5. J.Y. Chin, A.L. Ahmad, S.C. Low, Evolution of photocatalytic membrane for antibiotics degradation: perspectives and insights for sustainable environmental remediation. J. Water Process Eng. **51**, 103342 (2023). https://doi.org/10.1016/j.jwpe.2022.103342
6. S. Rana, A. Kumar, P. Dhiman, G.T. Mola, G. Sharma, C.W. Lai, Recent advances in photocatalytic removal of sulfonamide pollutants from waste water by semiconductor heterojunctions: a review. Mater. Chem. Today **30**, 101603 (2023). https://doi.org/10.1016/j.mtchem.2023.101603
7. M. Goudarzi, N. Mir, O. Amiri, M. Salavati-Niasari, Photocatalytic degradation of antibiotic using Ni-doped thallium(I) orthotungstate nanorods: hydrothermal synthesis and characterization. J. Alloy. Compd. **874**, 159856 (2021). https://doi.org/10.1016/j.jallcom.2021.159856
8. M.F. Lanjwani, M. Tuzen, M.Y. Khuhawar, T.A. Saleh, Trends in photocatalytic degradation of organic dye pollutants using nanoparticles: a review. Inorg. Chem. Commun. **159**, 111613 (2024). https://doi.org/10.1016/j.inoche.2023.111613
9. G.F.I. Toki, N. Sharif, A. Hossen, A. Rahman, R. Mia, R. Repon, S. Sk, T.M. Almutairi, M.K. Hossain, Sustainable coloration and analysis of cellulosic viscose fabric incorporating Rosa rubiginosa extraction and pre-mordanting approaches. Mater. Today Commun. **38**, 108068 (2024). https://doi.org/10.1016/j.mtcomm.2024.108068
10. S. Ullah, Q. Li, R. Ullah, S. Anwar, M.F. Hameed, M. Zhu, Facile synthesis of water-soluble silver nanoclusters for the photocatalytic degradation of dyes by multivariate optimization approach. Nanoscale Adv. **5**, 3326–3335 (2023). https://doi.org/10.1039/D3NA00227F
11. A. Ahmad, S.H. Mohd-Setapar, C.S. Chuong, A. Khatoon, W.A. Wani, R. Kumar, M. Rafatullah, Recent advances in new generation dye removal technologies: novel search for approaches to reprocess wastewater. RSC Adv. **5**, 30801–30818 (2015). https://doi.org/10.1039/C4RA16959J
12. R. Rashid, I. Shafiq, P. Akhter, M.J. Iqbal, M. Hussain, A state-of-the-art review on wastewater treatment techniques: the effectiveness of adsorption method. Environ. Sci. Pollut. Res. **28**, 9050–9066 (2021). https://doi.org/10.1007/s11356-021-12395-x
13. H. Wu, L. Li, S. Wang, N. Zhu, Z. Li, L. Zhao, Y. Wang, Recent advances of semiconductor photocatalysis for water pollutant treatment: mechanisms, materials and applications. Phys. Chem. Chem. Phys. **25**, 25899–25924 (2023). https://doi.org/10.1039/D3CP03391K
14. A. Balapure, J.R. Dutta, R. Ganesan, Recent advances in semiconductor heterojunctions: a detailed review of the fundamentals of photocatalysis, charge transfer mechanism and materials. RSC Appl. Interfaces (2024). https://doi.org/10.1039/D3LF00126A
15. T. Wang, P.D. Dissanayake, M. Sun, Z. Tao, W. Han, N. An, Q. Gu, D. Xia, B. Tian, Y.S. Ok, J. Shang, Adsorption and visible-light photocatalytic degradation of organic pollutants by functionalized biochar: role of iodine doping and reactive species. Environ. Res. **197**, 111026 (2021). https://doi.org/10.1016/j.envres.2021.111026

16. J. Feng, X. Ran, L. Wang, B. Xiao, L. Lei, J. Zhu, Z. Liu, X. Xi, G. Feng, Z. Dai, R. Li, The synergistic effect of adsorption-photocatalysis for removal of organic pollutants on mesoporous Cu2V2O7/Cu3V2O8/g-C3N4 heterojunction. Int. J. Mol. Sci. **23**, 14264 (2022). https://doi.org/10.3390/ijms232214264
17. E. Jimenez Relinque, S.F. Lee, L. Plaza, M. Castellote, Synergetic adsorption–photocatalysis process for water treatment using TiO2 supported on waste stainless steel slag. Environ. Sci. Pollut. Res. **29**, 39712–39722 (2022). https://doi.org/10.1007/s11356-022-18728-8
18. B.Y. Balarabe, P. Maity, Visible light-driven complete photocatalytic oxidation of organic dye by plasmonic Au-$TiO_2$ nanocatalyst under batch and continuous flow condition. Colloids Surf., A **655**, 130247 (2022). https://doi.org/10.1016/j.colsurfa.2022.130247
19. K. Bano, S.K. Mittal, P.P. Singh, S. Kaushal, Sunlight driven photocatalytic degradation of organic pollutants using a $MnV_2O_6$/$BiVO_4$ heterojunction: mechanistic perception and degradation pathways. Nanoscale Adv. **3**, 6446–6458 (2021). https://doi.org/10.1039/D1NA00499A
20. A.B.A. Baig, V. Rathinam, J. Palaninathan, Photodegradation activity of yttrium-doped $SnO_2$ nanoparticles against methylene blue dye and antibacterial effects. Appl Water Sci **10**, 76 (2020). https://doi.org/10.1007/s13201-020-1143-1
21. S. Shen, T. Ke, D. Fang, D. Lin, N and S co-doping of $TiO_2$@C derived from in situ oxidation of $Ti_3C_2$ MXene for efficient persulfate activation and sulfamethoxazole degradation under visible light. Sep. Purif. Technol. **297**, 121460 (2022). https://doi.org/10.1016/j.seppur.2022.121460
22. P. Manojkumar, E. Lokeshkumar, A. Saikiran, B. Govardhanan, M. Ashok, N. Rameshbabu, Visible light photocatalytic activity of metal (Mo/V/W) doped porous $TiO_2$ coating fabricated on Cp-Ti by plasma electrolytic oxidation. J. Alloy. Compd. **825**, 154092 (2020). https://doi.org/10.1016/j.jallcom.2020.154092
23. Z. Chen, S. Yu, J. Liu, Y. Zhang, Y. Wang, J. Yu, M. Yuan, P. Zhang, W. Liu, J. Zhang, C, F co-doping Ag/$TiO_2$ with visible light photocatalytic performance toward degrading Rhodamine B. Environ. Res. **232**, 116311 (2023). https://doi.org/10.1016/j.envres.2023.116311
24. A. Rani, K. Singh, A.S. Patel, A. Chakraborti, S. Kumar, K. Ghosh, P. Sharma, Visible light driven photocatalysis of organic dyes using $SnO_2$ decorated $MoS_2$ nanocomposites. Chem. Phys. Lett. **738**, 136874 (2020). https://doi.org/10.1016/j.cplett.2019.136874
25. A. Khalid, P. Ahmad, A. Khan, A.A.H. Abdellatif, A.M. Abu-Dief, B.S. Al-Anzi, H.A. Almukhlifi, H.W. Alhamdi, A.M. Alanazi, O.A. Jefri, M.M. Alsowayigh, A.H. Alsehli, S.A. Alderhami, R. Ahmed, Development of CuO and CuO:$Zn^{2+}$ nano-oxides for dye degradation and pharmaceutical studies. Inorg. Chem. Commun. **160**, 111887 (2024). https://doi.org/10.1016/j.inoche.2023.111887
26. M.J. Abel, A. Pramothkumar, N. Senthilkumar, K. Jothivenkatachalam, P.F.H. Inbaraj, J.J. Prince, Flake-like $CuMn_2O_4$ nanoparticles synthesized via co-precipitation method for photocatalytic activity. Physica B: Condensed Matter **572**, 117–124 (2019). https://doi.org/10.1016/j.physb.2019.07.047
27. A. Sobhani, Hydrothermal synthesis of $CuMn_2O_4$/CuO nanocomposite without capping agent and study its photocatalytic activity for elimination of dye pollution. Int. J. Hydrogen Energy **47**, 20138–20152 (2022). https://doi.org/10.1016/j.ijhydene.2022.04.149
28. B. Yu, H. Chang, W. Wei, H. Yu, Z. Chen, X. Cheng, D. Chen, Y. Jin, D. Han, W. Xu, Highly effective removal of ciprofloxacin antibiotic from water by magnetic metal–organic framework. Water **15**, 2531 (2023). https://doi.org/10.3390/w15142531
29. H. Sh, R.M. El-taweel, K.A. Alrefaey, A. Labena, I.S. Fahim, L.A. Said, A.G. Radwan, Enhanced removal of crystal violet using rawfava bean peels, its chemically activated carbon compared with commercial activated carbon. Case Stud. Chem. Environ. Eng. **9**, 100534 (2024). https://doi.org/10.1016/j.cscee.2023.100534
30. A. Habib, M. Ikram, A. Haider, A. Ul-Hamid, I. Shahzadi, J. Haider, M.B. Kanoun, S. Goumri-Said, W. Nabgan, Experimental and theoretical study of catalytic dye degradation and bactericidal potential of multiple phase Bi and $MoS_2$ doped $SnO_2$ quantum dots. RSC Adv. **13**, 10861–10872 (2023)
31. R. Verma, K.R.B. Singh, R. Verma, J. Singh, Nanoengineered parallelogram-$NiFe_2O_4$/rGO nanocomposite-based biosensing interface for highly efficient electrochemical detection of neurodegenerative disorders via dopamine monitoring. RSC Appl. Interfaces (2024). https://doi.org/10.1039/D3LF00153A
32. S. Koppala, R. Balan, I. Banerjee, K. Li, L. Xu, H. Liu, D.K. Kumar, K.R. Reddy, V. Sadhu, Room temperature synthesis of novel worm like tin oxide nanoparticles for photocatalytic degradation of organic pollutants. Mater. Sci. Energy Technol. **4**, 113–118 (2021). https://doi.org/10.1016/j.mset.2021.03.002
33. X. Gao, G. Huang, H. Gao, C. Pan, H. Wang, J. Yan, Y. Liu, H. Qiu, N. Ma, J. Gao, Facile fabrication of $Bi_2S_3$/$SnS_2$ heterojunction photocatalysts with efficient photocatalytic activity under visible light. J. Alloy. Compd. **674**, 98–108 (2016). https://doi.org/10.1016/j.jallcom.2016.03.031

34. J.A.C. Sackey, A.K.H. Nwanya, N. Bashir, J.B. Matinise, A.E. Ngilirabanga, E. Ameh, M. Coetsee, Maaza, Electrochemical properties of Euphorbia pulcherrima mediated copper oxide nanoparticles. Mater. Chem. Phys. **244**, 122714 (2020). https://doi.org/10.1016/j.matchemphys.2020.122714
35. M.J. Abel, A. Pramothkumar, N. Senthilkumar, K. Jothivenkatachalam, P.F.H. Inbaraj, J.J. Prince, Flake-like $CuMn_2O_4$ nanoparticles synthesized via co-precipitation method for photocatalytic activity. Physica B **572**, 117–124 (2019). https://doi.org/10.1016/j.physb.2019.07.047
36. J.H. Lim, S.M. Lee, H. Kim, H. Kim, J. Park, S. Jung, G. Park, J. Kim, J. Joo, Synergistic effect of Indium and Gallium co-doping on growth behavior and physical properties of hydrothermally grown ZnO nanorods. Sci. Rep. **7**, 41992 (2017). https://doi.org/10.1038/srep41992
37. K.M. Batoo, S. Kumar, C.G. Lee, Alimuddin: influence of Al doping on electrical properties of Ni–Cd nano ferrites. Curr. Appl. Phys. **9**, 826–832 (2009). https://doi.org/10.1016/j.cap.2008.08.001
38. X. Li, X. Cao, L. Xu, L. Liu, Y. Wang, C. Meng, Z. Wang, High dielectric constant in Al-doped ZnO ceramics using high pressure treated powders. J. Alloy. Compd. **657**, 90–94 (2016). https://doi.org/10.1016/j.jallcom.2015.10.079
39. M.A. Dar, K.M. Batoo, V. Verma, W.A. Siddiqui, R.K. Kotnala, Synthesis and characterization of nano-sized pure and Al-doped lithium ferrite having high value of dielectric constant. J. Alloy. Compd. **493**, 553–560 (2010). https://doi.org/10.1016/j.jallcom.2009.12.154
40. N. Komal, M.A. Mansoor, M. Mazhar, M. Sohail, Z. Malik, M. Anis-ur-Rehman, Effect of (Sm, In) doping on the electrical and thermal properties of $Sb_2Te_3$ microstructures. ACS Omega **8**, 9797–9806 (2023). https://doi.org/10.1021/acsomega.2c05859
41. M. Belghiti, K. Tanji, L. El Mersly, I. Lamsayety, K. Ouzaouit, H. Faqir, I. Benzakour, S. Rafqah, A. Outzourhit, Fast and non-selective photodegradation of basic yellow 28, malachite green, tetracycline, and sulfamethazine using a nanosized ZnO synthesized from zinc ore. React. Kinet. Mech. Catal. **135**, 2265–2278 (2022). https://doi.org/10.1007/s11144-022-02232-8
42. W. Han, D. Li, Y. Kong, W. Liu, W. Qin, S. Wang, X. Duan, High-performance photocatalytic peroxymonosulfate activation by carbon quantum dots via precise surface chemistry regulation: insight into the structure–function relations. J. Colloid Interface Sci. **646**, 633–648 (2023). https://doi.org/10.1016/j.jcis.2023.05.092
43. X. Huang, C. Xiao, Y. Tang, Removal of azo dye RY17 from wastewater using g-$C_3N_4$@CoO nanocomposite photocatalyst: synthesis, optical and electrochemical characterization and performance evaluation. Int. J. Electrochem. Sci. **18**, 100279 (2023). https://doi.org/10.1016/j.ijoes.2023.100279
44. M.R. Alotaibi, Synthesis and characterization of copper manganate-decorated zirconium dioxide nanoparticles and its photocatalytic application. Appl. Nanosci. **13**, 5579–5588 (2023). https://doi.org/10.1007/s13204-023-02774-w
45. S. Chabri, A. Dhara, B. Show, D. Adak, A. Sinha, N. Mukherjee, Mesoporous CuO–ZnO p–n heterojunction based nanocomposites with high specific surface area for enhanced photocatalysis and electrochemical sensing. Catal. Sci. Technol. **6**, 3238–3252 (2016). https://doi.org/10.1039/C5CY01573A
46. H. Leelavathi, R. Muralidharan, N. Abirami, S. Tamizharasan, S. Sankeetha, A. Kumarasamy, R. Arulmozhi, Construction of step-scheme g-$C_3N_4$/Co/ZnO heterojunction photocatalyst for aerobic photocatalytic degradation of synthetic wastewater. Colloids Surf., A **656**, 130449 (2023). https://doi.org/10.1016/j.colsurfa.2022.130449
47. S. Sankeetha, R. Muralidharan, N. Abirami, H. Leelavathi, S. Tamizharasan, A. Kumarasamy, R. Arulmozhi, A novel Ni doped $BaTiO_3$/h-BN nanocomposite for visible light assisted enhanced photocatalytic degradation of textile effluent and phytotoxicity evaluation. Ceram. Int. **49**, 6125–6138 (2023). https://doi.org/10.1016/j.ceramint.2022.10.100
48. H. Leelavathi, R. Muralidharan, N. Abirami, R. Arulmozhi, Development of Z-scheme bimetallic tungstate-supported nitrogen deficient g-$C_3N_4$ heterojunction for the treatment of refractory pharmaceutical pollutants. New J. Chem. **47**, 7774–7789 (2023). https://doi.org/10.1039/D3NJ00660C
49. J. Puneetha, N. Kottam, A. Rathna, Investigation of photocatalytic degradation of crystal violet and its correlation with bandgap in ZnO and ZnO/GO nanohybrid. Inorg. Chem. Commun. **125**, 108460 (2021). https://doi.org/10.1016/j.inoche.2021.108460
50. S. Gouthamsri, M. Ramanaiah, K. Basavaiah, K.J. Rao, Zr-doped ZnO nanohybrid via glycine mediated sol–gel approach as benign supporter for degradation of Crystal violet and antibacterial performance. Results Chem. **6**, 101080 (2023). https://doi.org/10.1016/j.rechem.2023.101080
51. M. Kaur, D. Prasher, V. Dhiman, P. Murugesan, D. Ghosh, R. Sharma, Green energy induced photocatalytic decomposition of methylene blue and crystal violet dyes by strontium doped tin oxide nanoparticles and its antibacterial activity. Physica B **661**, 414924 (2023). https://doi.org/10.1016/j.physb.2023.414924
52. I. Misbah, F. Bibi, S. Majid, K. Kamal, B. Jilani, Z. Taj, M. Nazeer, Iqbal, Enhanced visible light-driven photocatalytic

degradation of crystal violet dye using Cr doped $BaFe_{12}O_{19}$ prepared via facile micro-emulsion route. J. Saudi Chem. Soc. **26**, 101533 (2022). https://doi.org/10.1016/j.jscs.2022.101533

53. S. Sezer, P. Demircivi, N.E. Aydin, G.N. Saygili, Photocatalytic degradation of ciprofloxacin by using tannin-doped $BaTiO_3$ catalyst. J. Photochem. Photobiol., A **451**, 115468 (2024). https://doi.org/10.1016/j.jphotochem.2024.115468
54. X. Yu, J. Zhang, J. Zhang, J. Niu, J. Zhao, Y. Wei, B. Yao, Photocatalytic degradation of ciprofloxacin using Zn-doped $Cu_2O$ particles: analysis of degradation pathways and intermediates. Chem. Eng. J. **374**, 316–327 (2019). https://doi.org/10.1016/j.cej.2019.05.177
55. L.T. Nguyen, H.T. Nguyen, T.-D. Pham, T.D. Tran, H.T. Chu, H.T. Dang, V.-H. Nguyen, K.M. Nguyen, T.T. Pham, B.V. der Bruggen, UV–visible light driven photocatalytic degradation of ciprofoxacin by N, S co-doped $Ti_O2$: the effect of operational parameters. Top. Catal. **63**, 985–995 (2020). https://doi.org/10.1007/s11244-020-01319-7

**Publisher's Note** Springer Nature remains neutral with regard to jurisdictional claims in published maps and institutional affiliations.

Springer Nature or its licensor (e.g. a society or other partner) holds exclusive rights to this article under a publishing agreement with the author(s) or other rightsholder(s); author self-archiving of the accepted manuscript version of this article is solely governed by the terms of such publishing agreement and applicable law.